Catalysis Today 283 (2017) 134–143

Contents lists available at ScienceDirect

Catalysis Today

journal homepage: www.elsevier.com/locate/cattod

Surface composition changes of CuNi-ZrO_2 during methane decomposition: An *operando* NAP-XPS and density functional study

Astrid Wolfbeisser[a], Gábor Kovács[b], Sergey M. Kozlov[b], Karin Föttinger[a], Johannes Bernardi[c], Bernhard Klötzer[d], Konstantin M. Neyman[b,e,**], Günther Rupprechter[a,*]

[a] Institute of Materials Chemistry, Technische Universität Wien, Getreidemarkt 9/BC/01, 1060 Vienna, Austria
[b] Departament de Ciència de Materials i Química Física and Institut de Química Teòrica i Computacional (IQTCUB), Universitat de Barcelona, C/Martí i Franquès 1, 08028 Barcelona, Spain
[c] University Service Center for Transmission Electron Microscopy, Technische Universität Wien, Wiedner Hauptstraße 8-10, 1040 Vienna, Austria
[d] Institute of Physical Chemistry, University of Innsbruck, Innrain 52a, 6020 Innsbruck, Austria
[e] Institució Catalana de Recerca i Estudis Avançats (ICREA), 08010 Barcelona, Spain

ARTICLE INFO

Article history:
Received 15 December 2015
Received in revised form 29 March 2016
Accepted 13 April 2016
Available online 26 May 2016

Keywords:
Heterogeneous catalysis
Nanoparticles
Surface spectroscopy
Density functional theory
Methane
Bimetallics

ABSTRACT

Bimetallic CuNi nanoparticles of various nominal compositions (1:3, 1:1, 3:1) supported on ZrO_2 were employed for operando spectroscopy and theoretical studies of stable surface compositions under reaction conditions of catalytic methane decomposition up to 500 °C. The addition of Cu was intended to increase the coke resistance of the catalyst. After synthesis and (in situ) reduction the CuNi nanoparticles were characterized by HR-TEM/EDX, XRD, FTIR (using CO as probe molecule) and NAP-XPS, all indicating a Cu rich surface, even when the overall nanoparticle composition was rich in Ni. Density functional (DF) theory modelling, applying a recently developed computational protocol based on the construction of topological energy expressions, confirmed that in any studied composition Cu segregation on surface positions is an energetically favourable process, with Cu preferentially occupying corner and edge sites. Ni is present on terraces only when not enough Cu atoms are available to occupy all surface sites.

When the catalysts were applied for methane decomposition they were inactive at low temperature but became active above 425 °C. Synchrotron-based *operando* NAP-XPS indicated segregation of Ni on the nanoparticle surface when reactivity set in for CuNi-ZrO_2. Under these conditions C 1s core level spectra revealed the presence of various carbonaceous species at the surface. DF calculations indicated that both the increase in temperature and especially the adsorption of CH_x groups (x = 0-3) induce the segregation of Ni atoms on the surface, with CH_3 providing the lowest and C the highest driving force.

Combined operando and theoretical studies clearly indicate that, independent of the initial surface composition after synthesis and reduction, the CuNi-ZrO_2 catalyst adopts a specific Ni rich surface under reaction conditions. Based on these findings we provide an explanation why Cu rich bimetallic systems show improved coke resistance.

1. Introduction

Bimetallic nanoparticles are of high interest in heterogeneous catalysis because their properties can be very different from the properties of the constituent metals. The alloying may create a variety of atomic arrangements with quite distinct and different electronic structures [1–3], such as (partly) alloyed nanoparticles and core-shell structures.

Ni-based catalysts are employed in a variety of reactions, with methane reforming being among the most important. However, Ni catalysts are prone to deactivation by coking, which can be hindered by the addition of a second metal such as Au [4,5] or Cu [6–11]. Since neighbouring Ni atoms are necessary for coke formation, the coking resistance can be improved by replacing the Ni neighbours by Au or Cu atoms (ensemble effect) or by simply

* Corresponding author.
** Corresponding author at: Departament de Ciència de Materials i Química Física and Institut de Química Teòrica i Computacional (IQTCUB), Universitat de Barcelona, C/Martí i Franquès 1, 08028 Barcelona, Spain.
E-mail addresses: konstantin.neyman@icrea.cat (K.M. Neyman), guenther.rupprechter@tuwien.ac.at (G. Rupprechter).

http://dx.doi.org/10.1016/j.cattod.2016.04.022

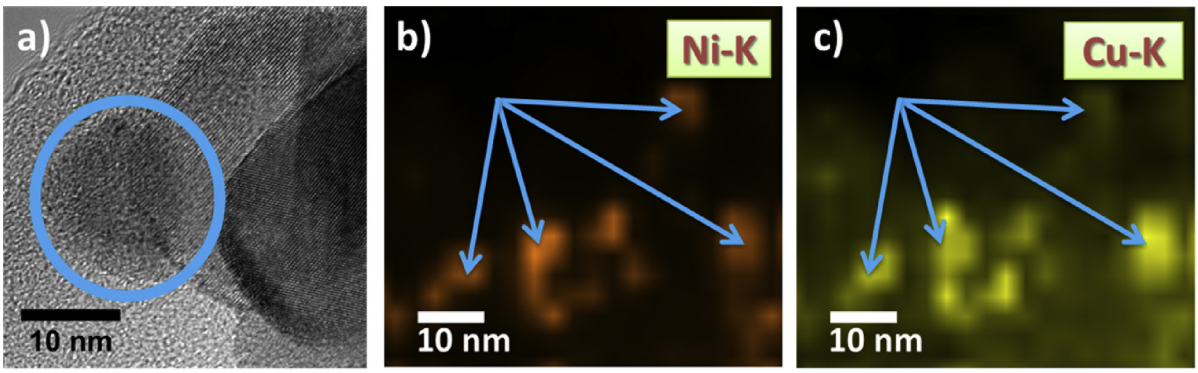

Fig. 1. a) TEM image of 11CuNi-ZrO_2. The particle inside the circle was identified via EDX as containing both Ni and Cu. Elemental map for K edge energies of b) Ni and c) Cu recorded on 11CuNi-ZrO_2: The particles contain both Ni and Cu.
Adapted from [11]-Published by The Royal Society of Chemistry.

physically blocking Ni steps/edges by Au or Cu. In the current work, copper was chosen as alloying component because of its lower price compared to gold and the strong tendency of the latter to sinter.

The production of "clean" hydrogen is an important technological challenge hindering the emergence of more efficient and environmentally friendly energy technologies. When H_2 is produced via steam reforming of methane [12–14] or partial oxidation the "by-product" CO may constitute a problem (e.g. for PEM fuel cells) and must be removed (e.g. by water gas shift and preferential oxidation, CO-PROX). One alternative route to avoid CO formation is the direct catalytic decomposition of methane (in the absence of water, air or oxygen) producing hydrogen and, as a by-product, carbon. Clearly, this route can only be feasible when the produced carbon does not deactivate the catalyst. Carbon may be present in the form of layers, filaments, fibres or nanotubes, with nanocarbons [15–17] being of particular interest. Li et al. [18] reviewed this topic discussing the effect of the nature of the catalyst and feed composition on the catalytic activity, stability and the morphology of the produced carbon. Since "coke" is a product of methane decomposition, we have utilized this reaction to evaluate the surface composition and coking resistance of CuNi nanoparticles, i.e. whether hydrogen production can be maintained despite carbon formation.

In addition to the dissociation of methane (1.1), reactions of methane with hydroxyl groups (1.2) or oxygen from the support (1.3) may occur during methane decomposition, lowering the amount of carbon deposited (the index *s* indicating that the molecule/fragment is adsorbed on the surface).

$$CH_4 \leftrightarrow C + 2H_2 \quad (1.1)$$

$$CH_4 + 2OH_s \rightarrow CO_2 + 3H_2 \quad (1.2)$$

$$CH_4 + 2O_s \rightarrow CO_2 + 2H_2 \quad (1.3)$$

Using density functional (DF) method Liao et al. [19] calculated dissociation enthalpies and activation energies for the sequential dehydrogenation ($CH_{x,s} \rightarrow CH_{x-1,s} + H_s$; x = 4 to 1) and oxygen-assisted dissociation of methane on small cluster models of various transition metals. Whereas Ni was found to be one of the most efficient catalysts for methane dissociation, the total dissociation of methane on Cu and other coinage metals was found to be strongly endothermic. The presence of adsorbed oxygen, however, promoted methane dissociation [19,20] by increasing the energy of hydrogen adsorption [20]. Furthermore, compared to other transition metals, the ability of Cu to catalyze the reaction of carbon produced via (1.1) with surface oxygen is rather high [20].

Apart from the ability to prepare CuNi nanoparticles it is also important to evaluate their in situ stability under reaction conditions, i.e. high temperatures and in a reactive gas atmosphere. It is well accepted that catalysts often change under reaction conditions [3,21–24]. Some of us have previously studied CH_4 and methanol reforming activities and selectivities on Ni, Cu and Pd-based catalysts by combining in situ (operando) spectroscopic techniques such as X-ray photoelectron (XPS), infrared (FTIR) and X-ray absorption (XAS) spectroscopy [10,11,25–27]. FTIR of adsorbed CO suggested that CuNi alloy formation occurred during catalyst reduction and XAS indicated about 100 °C lower reduction temperature of NiO in the bimetallic catalyst as compared to the monometallic one [10]. IR studies of methane decomposition at 500 °C demonstrated that the addition of Cu to Ni strongly reduced the coking occurring preferentially on nickel, while maintaining methane decomposition activity [10]. In situ synchrotron-based near atmospheric pressure (NAP-)XPS revealed reaction-induced changes in the nanoparticle surface composition. Depth profiling was performed to visualize surface segregation processes by variation of the incident photon energy (creating photoelectrons with specific kinetic energies) [11].

Herein, we have re-evaluated the surface structural changes and stability of supported CuNi bimetallic nanoparticles under reaction conditions of methane decomposition. We focus on *operando* NAP-XP spectroscopy, in order to identify the catalytically relevant surface configurations of the nanoparticles. Most importantly, density functional calculations have been employed to characterize the surface composition of the as-prepared (reduced) bimetallic nanoparticles, as well as that of nanoparticles covered by CH_x species (x = 0 to 3) under reaction conditions. The simulations show that at low temperatures and when adsorbates are absent, Cu segregates on the surface of Cu-Ni nanoparticles in thermodynamic equilibrium. However, the surface composition may change due to temperature induced disorder, and especially, the presence of adsorbed CH_x species, which facilitate the emergence of Ni on the surface. Based on the current analysis favourable configurations for CuNi nanoparticles with improved catalytic performance are suggested.

2. Materials and methods

Bimetallic CuNi-ZrO_2 catalysts were synthesized by impregnation of ZrO_2 using nitrate precursor salts. Before impregnation, commercial $Zr(OH)_4$ (MEL chemicals XZO 880/01) was calcined at a heating rate of 2 °C/min from room temperature to 700 °C and kept at this temperature for 2 h. After calcination the zirconia support exhibits a specific surface area of 36.6 m^2/g [10]. For co-impregnation $Cu(NO_3)_2\,3H_2O$ (Fluka, p.a.) and $Ni(NO_3)_2\,6H_2O$ (Merck, p.a.) were mixed to obtain Cu:Ni molar ratios of 1:0, 3:1, 1:1, 1:3 and 0:1. The nitrates were dissolved in water, and the proper amount of ZrO_2 powder was suspended in these solutions.

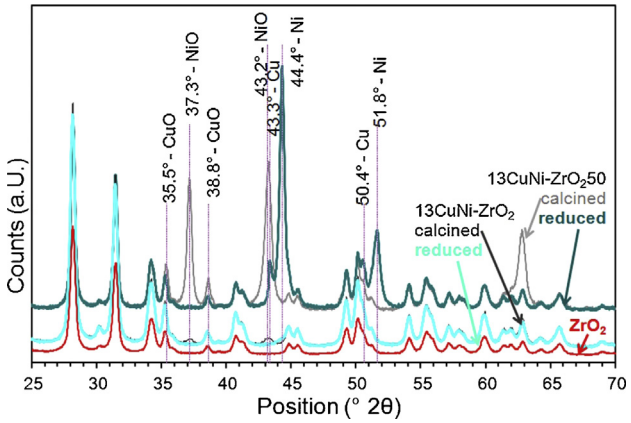

Fig. 2. XRD patterns of ZrO_2, 13CuNi-ZrO_2 and 13 CuNi-$ZrO_2$50.

The solutions contained as much metal nitrate to obtain 5 wt% metal loading. For XPS investigations an additional sample with 50 wt% was synthesized with a Cu:Ni ratio of 1:3. In the following, the samples containing 5 wt% metal loading are labelled as Ni-ZrO_2, 13CuNi-ZrO_2, 11CuNi-ZrO_2, 31CuNi-ZrO_2 and Cu-ZrO_2, with the numbers providing the Cu:Ni ratio. The sample containing 50 wt% metal loading is denoted as 13CuNi-$ZrO_2$50.

Transmission electron microscopy (TEM) was utilized to obtain information about the size, morphology and distribution of the metal particles on the zirconia support. For TEM measurements the sample was deposited on a carbon-coated Au grid. The catalyst was ex-situ oxidized at 500 °C and reduced at 400 °C prior to the experiment. TEM measurements were performed using an analytical TECNAI F20 field emission TEM operated at 200 kV equipped with an energy dispersive X-ray detector (EDX). EDX was used to identify the CuNi particles on the support materials.

X-ray diffraction (XRD) studies were carried out on an XPERT-PRO diffractometer with Cu Kα radiation operating at 40 kV and 40 mA with a 2θ scanning from 5 to 90° and a step size of 0.02°.

IR spectra were recorded in transmission using a Bruker Vertex 70 spectrometer with a mercury cadmium telluride (MTC) detector. Samples were pressed to small discs and placed in the IR cell. All infrared spectra were collected at a resolution of 4 cm^{-1} in the 4000-900 cm^{-1} range by averaging 128 scans to achieve good signal to noise ratio. The oxidation treatment was carried out in the IR cell by heating from room temperature to 500 °C at 10 K min^{-1} under 100 mbar O_2 pressure and holding the temperature for 1 h. Then, the IR cell was evacuated, the sample was cooled down to 300 °C and heated in 5 mbar H_2 and 900 mbar N_2 to 400 °C. The temperature was maintained for 30 min in the reducing gas mixture and another 30 min in vacuum before cooling down to room temperature. In order to reveal surface oxidation states by using CO as a probe molecule, FTIR spectra were recorded before and after exposure to 5 mbar CO at 30 °C. In a second experiment, 5 mbar CH_4 and 900 mbar N_2 were filled into the chamber after the same pretreatment procedure and the sample was heated with 2 °C/min up to 500 °C, with simultaneously recording FTIR spectra.

Temperature programmed methane decomposition (TPMd) experiments were performed in a quartz flow reactor. Part of the effluent was directed to a mass spectrometer (Pfeiffer QMS 200) via a differentially pumped capillary, detecting H_2, CO, CO_2 and CH_4. 50 mg catalyst were loaded into the glass reactor in-between two plugs of quartz wool. The catalysts were oxidized at 500 °C and reduced at 400 °C prior to the reaction. Then, the samples were heated up to 500 °C and subsequently cooled to 300 °C in a mixture of 5% CH_4 and 95% Ar with a total flow of 50 ml/min. The heating and cooling rate was set to 5 °C/min and the heating-cooling cycle was repeated twice. After the TPMd experiment the sample was cooled to room temperature in Ar.

In situ synchrotron-based near atmospheric pressure NAP-XPS experiments were carried out at the ISSIS-PGM beamline at the Helmholtz-Zentrum Berlin using a high pressure XPS station constructed at FHI Berlin [28]. In brief, the setup uses a differentially pumped electrostatic lens system and a SPECS hemispherical electron analyzer. The sample was placed inside the reaction cell with adjustable gas flows and a total pressure up to a few mbar. The composition of the gas phase was analyzed by MS. Heating was done by an IR laser from the sample back. The sample was in situ oxidized in 0.1 mbar O_2 at 300 °C, since reaching 500 °C was not possible in this experimental setup, and reduced in 0.25 mbar H_2 at 400 °C prior to exposure to 0.25 mbar CH_4 at temperatures ranging from 250 °C to 450 °C.

The catalyst 13CuNi-$ZrO_2$50 with 50 wt% total metal loading (which prevented sample charging) was used for the XPS experiments. The calcined powder was pressed onto a copper plate and reduced at 500 °C prior to placing it into the in situ reaction cell. Measurements were performed at photon energies of 1100 eV for the Cu 2p, 1010 eV for the Ni 2p and 425 eV for the C 1s XP spectra, yielding 150 eV photoelectron kinetic energy. For depth profiling the photon energies were varied to additionally obtain photoelectron kinetic energies of 350 eV and 550 eV. All spectra were corrected for synchrotron beam current, incident photon flux and energy dependent photo-ionization cross sections [29]. Binding energies (BEs) were referenced to the Fermi edge recorded after each core-level measurement. The measured signal envelopes were fitted with Gauss-Lorentzian peaks by using the software Casa XPS after subtraction of a Shirley background.

Electronic structure calculations of Cu-Ni nanoparticles (NPs) have been performed using the periodic plane-wave code VASP [30]. We used the PBE [31] exchange-correlation functional considered as one of the most appropriate among common functionals for the description of transition metals [32]. The projector augmented wave approach was applied to treat the interaction between valence and core electrons. The electron density was smeared by 0.1 eV using the first-order method of Methfessel and Paxton [33]; finally, energies of converged calculations were extrapolated to the zero smearing. All calculations were performed only at the Γ-point in the reciprocal space. The relaxation of all atoms was allowed during the geometry optimization until forces on each atom became less than 0.2 eV/nm. The minimal separation between NPs exceeded 0.7 nm, at which the interaction between adjacent NPs was found to be negligible [34,35]. Spin polarized calculations have been carried out throughout, and all gas phase CH_x references have been taken into account in the most stable spin state. The adsorption energy E_{ads} of CH_x groups on the $Cu_{70}Ni_{70}$ nanoparticle surface is defined by the total energies E as follows

$$E_{ads} = E(CH_x/Cu_{70}Ni_{70}) - [E(Cu_{70}Ni_{70}) + E(CH_x)].$$

3. Results and discussion

3.1. Characterization of bimetallic catalysts

In order to confirm that CuNi alloy nanoparticles indeed formed upon catalyst pre-treatment, different ex situ and in situ methods were applied to the catalyst before exposure to methane.

Fig. 1 shows a transmission electron micrograph of 11CuNi-ZrO_2 after ex situ reduction. The size of the ZrO_2 particles was between 50 and 100 nm, whereas the polycrystalline metal particles were about 20 nm in diameter. Elemental maps recorded by EDX detection showed that those particles contain both Cu and Ni. Since the (reduced) sample was exposed to air between reduction and

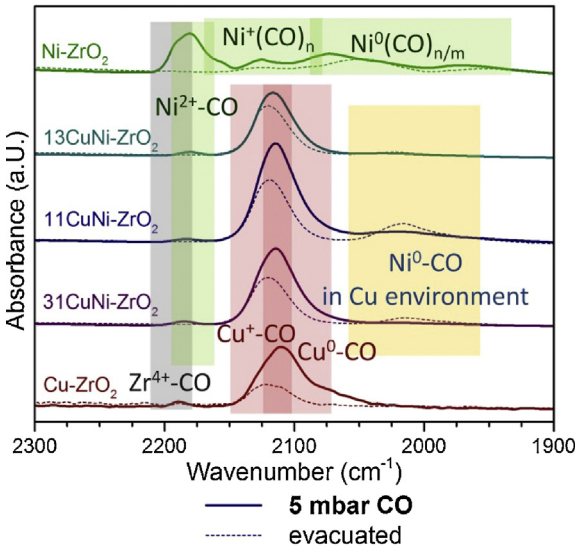

Fig. 3. Infrared spectra of reduced catalysts in 5 mbar CO pressure (solid lines) and after evacuation (dashed lines) at room temperature.
Adapted from [10].

transmission electron microscopy, the CuNi particles are expected to be (partially) reoxidized.

XRD patterns of the pure ZrO_2 support and of 13CuNi-ZrO_2 and 13CuNi-$ZrO_2$50, both after calcination and after ex situ reduction at 400 °C, are shown in Fig. 2. All display monoclinic ZrO_2 reflections.

Bulk CuO exhibits reflections at 35.5 and 38.8°, very close to those of monoclinic ZrO_2. These reflections loose intensity after reduction. The intensity of the characteristic reflections of NiO at 37.7° and 43.2° nearly vanished after reduction of both 13CuNi-ZrO_2 and 13CuNi-$ZrO_2$50. However, due to partial surface reoxidation upon air exposure small or amorphous NiO crystallites were likely present [10]. The reflections at 44.4° and 51.8° appearing after reduction are attributed to metallic Ni and shoulders at 43.3° and 50.4° are attributed to metallic Cu. Assignment of alloyed CuNi crystallites as reported for silica supported CuNi [36] was not possible because of overlap with reflections of monoclinic zirconia. Thus, XRD suggests that the catalyst consists of monoclinic ZrO_2 and both metallic and oxidized Cu and Ni after reduction (and air transport to XRD).

The exact distribution of these phases cannot be deduced from (bulk sensitive) XRD. However, even when large monometallic particles were additionally present in 13CuNi-$ZrO_2$50 their effect was minor. Cu particles would have very low activity and also large Ni particles (with low dispersion) would have only a minor contribution to the overall reaction rate. With respect to the XPS measurements presented below, the monometallic particles with low dispersion would also not contribute significantly.

X-ray absorption Cu K edge and Ni K edge spectra recorded on 11CuNi-ZrO_2, as well as comparison with monometallic Ni-ZrO_2 and monometallic Cu-ZrO_2, were shown in [10]. While NiO reduction of the monometallic Ni-ZrO_2 catalyst started only at about 390 °C, on the bimetallic CuNi catalyst reduction of NiO already set in at about 230 °C, indicating CuNi alloy formation. The reduction temperature of CuO in the bimetallic catalyst (160 °C) was also lower compared to monometallic Cu-ZrO_2 (290 °C).

In addition to these established bulk-sensitive methods, more surface-sensitive methods such as in situ XPS and FTIR spectroscopy were applied in order to examine surface alloy formation.

FTIR spectra of room temperature CO adsorption on catalyst samples after reduction at 400 °C are shown in Fig. 3. Besides bands of CO on reduced Cu and Ni, bands of CO on oxidized Cu and oxidized Ni species are present, again indicating incomplete reduction. On the monometallic Ni-ZrO_2 sample several bands appeared, which are attributed to carbonyls on Ni^0 and Ni^+ (at 2075 cm^{-1} [37–43] and 2125 and 2163 cm^{-1} [38–40,42,44,45], respectively) as described in detail in [10]. On the copper containing samples the much weaker CO interaction with reduced Cu^0 appearing below 2110 cm^{-1} [46–49] is observed in addition to the Cu^+-CO band, which was reported around 2120–2143 cm^{-1} [46–48]. CO on reduced Cu-ZrO_2 shows (beside the Zr^{4+}-CO interaction at 2190 cm^{-1} [10,50–52]) only one peak around 2111 cm^{-1} consisting both of Cu^0-CO and Cu^+-CO contributions, which shifts to 2123 cm^{-1} after evacuation, with the dominant contribution from the more stable Cu^+-CO complex.

Upon alloying Cu and Ni, the Ni^0—CO peak, which is located at about 2070 cm^{-1} in 5 mbar CO and at about 2050 cm^{-1} upon evacuation on Ni-ZrO_2, red-shifts by approximately 50–70 cm^{-1} to 2012–2023 cm^{-1} on the bimetallic samples (Fig. 3). The CO bands on CuNi alloy were indeed reported at about 40 cm^{-1} lower frequencies than on pure Ni [41,53]. In line with the current results, Dalmon et al. [40] had observed adsorbed Ni-CO at 2058 cm^{-1} on monometallic nickel, at 2028 cm^{-1} on a 36.6 % and at 2005 cm^{-1} on a 72 % copper containing alloy. Our theoretical analysis was able to reproduce the experimentally observed shifts in the CO stretching vibration frequencies (ca. 60 cm^{-1} red shift was calculated between pure Ni and Cu-Ni alloyed NPs). Based on the observation that there is no shift in the Cu^+-CO vibration with composition one can conclude that Ni seems to interact with Cu^0, but not with Cu^+. Even more important, on the bimetallic samples the peaks attributed to CO interaction with copper species are much stronger than those attributed to CO interacting with Ni, indicating that more Cu than Ni atoms are present on the bimetallic surface. Thus, FTIR spectroscopy showed that surface alloy formation takes place upon reduction but that the bimetallic surface is enriched in Cu.

Fig. 4 displays the Ni $2p_{3/2}$ and Cu $2p_{3/2}$ binding energy region of 13CuNi-$ZrO_2$50 during reduction in 0.25H_2 for 30 min. The peak at 854.3 eV in Fig. 4a) is attributed to NiO [54–57] and the peak appearing in reducing atmosphere at 852.6 eV is ascribed to metallic nickel [57,58]. One cannot distinguish between nickel interacting with copper and non-interacting with copper, due to the small chemical shift of about 0.2 eV, [59,60] which characterizes Ni alloyed with Cu. The insignificant chemical shift due to alloying is in line with the absence of notable charge transfer between Cu and Ni in simulations revealed by Bader analysis.

The small broad peak at 933.3 eV in Fig. 4b) is attributed to CuO [57,61–64] and the peak located at 932.3 eV is attributed to metallic Cu. Again, since the shift of alloyed Cu in CuNi is only ~0.2 eV [59,60], we could not differentiate between these species. Comparing the peak areas, we again observe that the surface is enriched in copper even though the nominal Cu:Ni ratio of this catalyst is 1:3.

For a better understanding of the structure of bimetallic Cu-Ni nanoalloys, theoretical calculations were carried out on model Cu-Ni NPs. We applied a recently developed computational protocol [65], which allows us to determine the optimal chemical ordering in several nanometre large bimetallic particles with the accuracy of density functional calculations. The latter method is based on the construction of topological energy expressions that depend solely on the atomic arrangement of the alloyed metals in a NP with a predetermined lattice. The applied topological expressions only involve some of the fundamental features of the NPs, such as the numbers of Cu atoms on terrace, edge, and corner positions together with the number of heterometallic Cu-Ni bonds. In these topology expressions an energy parameter, ε_i, called descriptor, corresponds to each of the aforementioned characteristics, related to either the surface segregation energy of Cu or the energy of Cu-Ni bond formation. The descriptors can be obtained via multiple linear regression fitting to the total energies calculated by DF methods

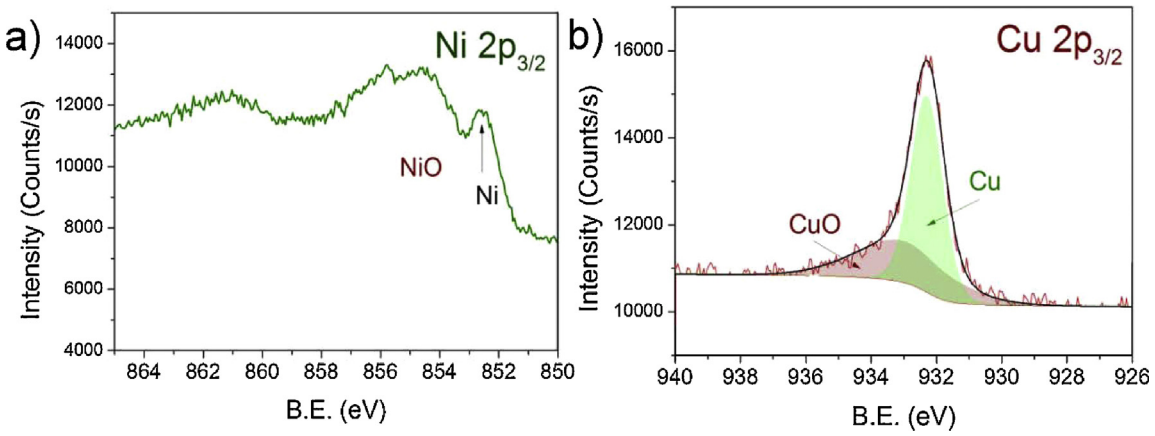

Fig. 4. XP spectra of a) Ni $2p_{3/2}$ and b) Cu $2p_{3/2}$ region of 13CuNi-$ZrO_2$50 in 0.25 mbar H_2 at 400 °C at a kinetic energy of the photoelectrons of 150 eV. Adapted from [11] –Published by The Royal Society of Chemistry.

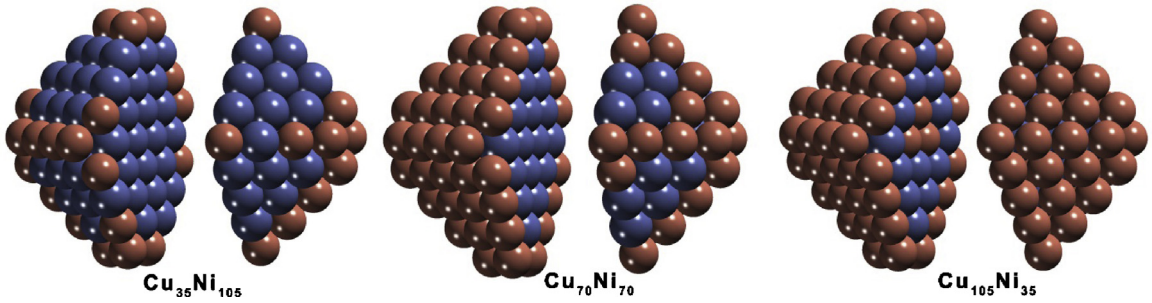

Fig. 5. Structures of $Cu_{35}Ni_{105}$ (1:3), $Cu_{70}Ni_{70}$ (1:1) and $Cu_{105}Ni_{35}$ (3:1) NPs with optimized chemical ordering. Cu atoms are displayed as redwood spheres, Ni atoms – blue spheres. (For interpretation of the references to colour in this figure legend, the reader is referred to the web version of this article.)

for a set of NP structures with different chemical ordering. A special type of Monte-Carlo simulations using the topologic energy expressions have been employed for the optimization of chemical ordering in the selected Cu-Ni NPs. Such simulations were also applied to obtain average NP properties in thermodynamic equilibrium at a given temperature. Note that thermodynamic quantities derived in such a way account only for degrees of freedom related to chemical (dis-) ordering, but lack other contributions such as atomic vibrations. The latter contributions can become more significant at higher temperature, which limits the applicability of the proposed analysis at elevated T.

The just outlined theoretical method has been applied to the analysis of chemical ordering in Cu-Ni nanoparticles with 1:3, 1:1 and 3:1 composition. Among the different ratios considered in the experiments throughout this study in this section we focus on the 1:3 (Ni-rich) composition, since this (nominal) composition is investigated by *operando* XPS measurements, which provide information on the surface structure. DF calculations have been carried out using the ca. 1.4 nm large $Cu_{35}Ni_{105}$, $Cu_{70}Ni_{70}$ and $Cu_{105}Ni_{35}$ NPs with truncated octahedral *fcc* structure. These nanoparticles have a large surface composed of 96 atoms and a small interior region made of 44 atoms only.

After the optimization of the chemical ordering in the Cu_XNi_{140-X} NPs, we can conclude that in any studied composition Cu segregation on surface positions is an energetically favourable process (Fig. 5). For instance, in the case of $Cu_{35}Ni_{105}$ the largest energy change corresponds to Cu segregation on 6-coodinated corner positions (−413 meV), whereas less substantial energy change is associated with Cu segregation on 7-coodinated edge (−300 meV) and 9-coordinated terrace (−193 meV) sites. The latter energy values clearly indicate that Cu is significantly stabilized on the surface relative to bulk positions. Accordingly, Cu prefers corner and edge sites to terrace positions, and Ni is present on the surface only when not enough Cu atoms are available to occupy all surface sites, as it can be seen in the minimum-energy structure obtained for $Cu_{70}Ni_{70}$ (Fig. 5).

A descriptor of +8 meV was obtained for Cu-Ni bond formation in $Cu_{35}Ni_{105}$, showing that the mixing of the two elements is not favourable during the alloying (the optimized descriptors for the other studied compositions are listed in the Supporting Information). The latter finding is consistent with results of the study by Panizon et al., in which DF-fitted atomistic potentials were used to show that intermixing of Cu and Ni is not favourable in lowest-energy NPs [66].

The descriptors obtained through the precise electronic structure calculations have then been used to predict the chemical ordering in the experimentally studied larger NPs of the same 1:3 composition. The appropriateness of such extrapolation is corroborated by our previous results obtained for Pd-Au [65] and Pt-Co nanoalloys [67], where we showed that descriptors for a particular composition hardly vary between different NP sizes.

In order to predict the structure of larger nanoparticles, we applied the descriptor set calculated for the $Cu_{35}Ni_{105}$ particle for the global optimization of the $Cu_{819}Ni_{2416}$ particle of ~6 nm size with truncated octahedral *fcc* structure and 1:3 composition. This nanoparticle contains 3235 atoms, of which 1020 are located on the surface. At 0 K, the bulk is purely Ni, whereas Cu occupies 80% of the surface (Fig. 6a). More precisely, all 24 corner and 156 edge sites are taken by Cu, whereas surface Ni atoms form islands on some of the terraces.

Nevertheless, studies of the thermodynamic equilibrium showed that the concentration of Ni on the surface gradually increases starting from 500 K (Fig. 6b). From 0 to 1000 K, Ni concentration on the surface almost gets doubled (from 20 to 35%),

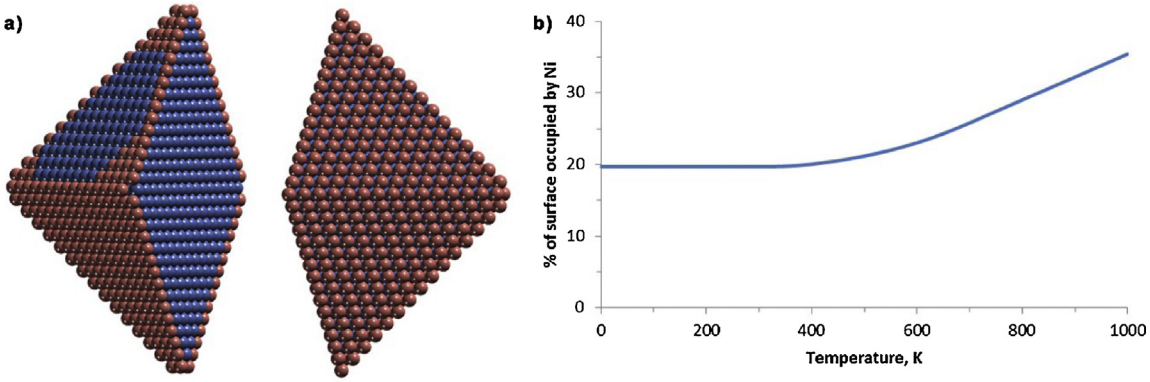

Fig. 6. a) Calculated equilibrium structure of the octahedral-like 6 nm large $Cu_{819}Ni_{2416}$ (1:3) particle at 0 K. Cu atoms are displayed as redwood spheres and Ni atoms are shown as blue spheres. b) Surface occupation by Ni atoms in the $Cu_{819}Ni_{2416}$ particle in thermodynamic equilibrium as a function of the temperature. (For interpretation of the references to colour in this figure legend, the reader is referred to the web version of this article.)

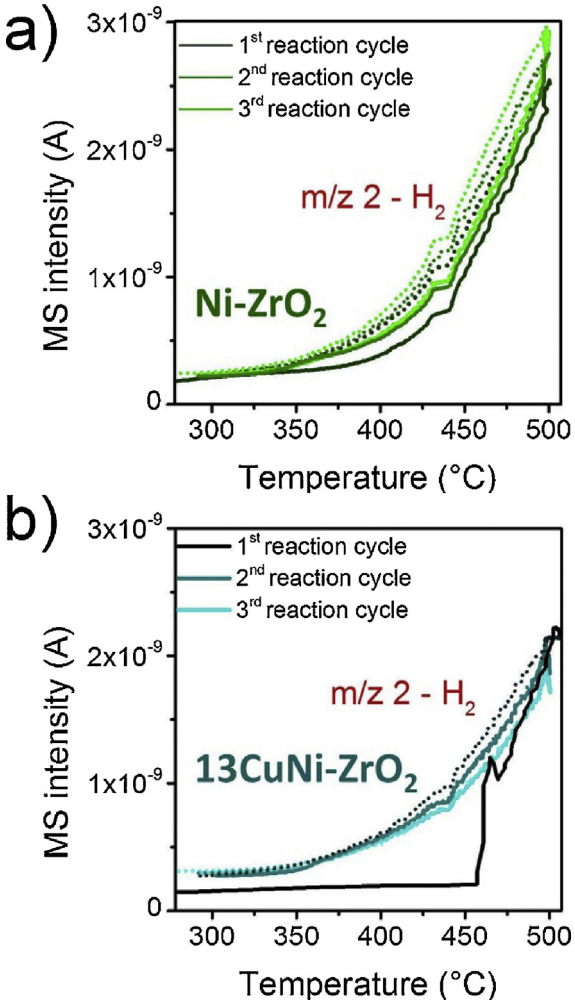

Fig. 7. Hydrogen evolution during methane decomposition on a) Ni-ZrO_2 and b) 13CuNi-ZrO_2. The samples were reduced at 400 °C followed by 3 heating-cooling cycles between 300 and 500 °C in CH_4/Ar. Solid lines show H_2 evolution during heating and dashed lines show H_2 evolution during cooling. The temperature was ramped at 5 °C/min.

Adapted from [11] —Published by The Royal Society of Chemistry.

which shows that higher temperatures facilitate Ni segregation on the surface.

We notice for completeness that the corresponding calculations have also been performed for Cu:Ni 1:1 and 3:1 compositions. The outer shell of both $Cu_{1638}Ni_{1637}$ (1:1) and $Cu_{2416}Ni_{819}$ (3:1) NPs is fully covered with Cu at 0 K, and even at 1000 K the Ni concentration on the surface was calculated to be only 15% and 5%, respectively. Therefore, all calculations are in coherence with the experimentally observed Cu-rich surfaces of the NPs after synthesis, even when the overall NP is rich in Ni.

3.2. Reaction induced surface segregation of Ni

The ability of the different catalysts for methane decomposition was examined mass spectroscopically by temperature programmed methane decomposition (TPMd). The results for Ni-ZrO_2 and 13CuNi-ZrO_2 are shown in Fig. 7. On Ni-ZrO_2 hydrogen production started at around 350 °C and increased with increasing temperature. Upon cooling the activity decreased reversibly. In a second heating cycle, the hydrogen production rate remained approximately the same as during the first cycle. Consequently, no deactivation of H_2 production activity was observed. Apart from H_2 formation, carbon dioxide evolution occurred during the first heating cycle in methane up to about 430 °C. The detected CO_2 likely originates from the reaction of methane with surface oxygen and/or carbonates on zirconia or with NiO present due to incomplete reduction. Note that CO_2 formation lowers the amount of deposited carbon on the catalyst surface.

Fig. 7b) shows the corresponding rate of hydrogen production for 13CuNi-ZrO_2. On this sample no catalytic activity was observed up to 460 °C but at higher temperature H_2 production increased rapidly, approaching the level of Ni-ZrO_2, which was again accompanied by a small amount of CO_2 evolution. Consecutive cycles were then very similar to those of Ni-ZrO_2, even at lower temperatures. This points to an irreversible surface modification of the bimetallic CuNi catalyst, which occurred during the first heating cycle in methane. This significantly changed the catalytic performance of the catalyst rendering it similar to Ni-ZrO_2. Indeed, at 500 °C 64% and 50% H_2 yield were reached over Ni-ZrO_2 and 13CuNi-ZrO_2, respectively. Using FTIR spectroscopy, performed during heating in 5 mbar CH_4 in N_2, a band at 1984 cm^{-1} was appearing (characteristic of Ni^0-CO and originating from CH_x interaction with lattice oxygen), suggesting Ni surface segregation. On the other bimetallic catalysts, 13CuNi-$ZrO_2$50 and 1:1 and 3:1 Cu:Ni, a similar trend was observed [11]. When performing TPMs over Cu-ZrO_2 almost no H_2 production was observed.

In order to monitor the surface modification processes *during* methane decomposition in more detail, *operando* NAP-XPS at millibar pressure was employed. The photon energy was adjusted to obtain photoelectron kinetic energies of 150 eV, 350 eV and 550 eV for each set of spectra of the relevant core level regions (Ni 2p, Cu

2p, C 1s). These kinetic energies correspond to inelastic mean free paths of 5, 8 and 10 Å, so that mainly the first 4, 6 and 8 layers were probed, respectively.

Fig. 8 shows XP spectra acquired during exposure to 0.25 mbar methane at 250 and 450 °C, immediately after reduction in 0.25 mbar hydrogen (for a photoelectron kinetic energy of 150 eV, i.e. for highest surface sensitivity probing mainly the first 4 layers). The methane conversion level was about 4% at 250 °C and 16% at 450 °C. The amount of metallic nickel increased with increasing reaction temperature (~1.7 times) whereas less metallic copper was observed at 450 °C compared to the starting conditions. Additionally, by increasing the temperature the metallic Cu peak became broader and shifted to slightly higher binding energy, which is in line with further Cu-Ni alloy formation. As shown in Fig. 8c) a number of different carbon-containing surface species was observed during methane decomposition. The total amount of carbonaceous species was strongly increasing when hydrogen production started between 425 and 450 °C. In particular, the peak at 284.8 eV, attributed to C with sp^2 hybridization [68–71] and indicating the formation of carbon nanotubes, strongly increased when 450 °C had been reached.

Fig. 8d) shows the XPS peak areas of metallic Cu and Ni, taking into account the elemental specific cross sections [29] and normalized to the XPS signals of the Zr 3d region. As discussed above, the surface is enriched in Cu after reduction as well as at the beginning of the reaction. Between 425 °C and 450 °C, however, while the hydrogen production onset was simultaneously observed via MS detection, the amount of surface Ni strongly increased as the amount of metallic Cu decreased. Studt et al. [72] reported that Ni may segregate on the surface due to higher binding strength towards CO. Since there is hardly any CO under the present conditions, we expect Ni to segregate closer to the surface at elevated temperature due to the presence of methane and/or, more probably, other carbonaceous species (see below).

When the corresponding spectra (Ni 2p, Cu 2p, C 1s; not shown) were acquired for a photoelectron kinetic energy of 350 eV and 550 eV (mainly probing the first 6 or 8 layers) the effect was found to be very similar, indicating that Ni segregation affects several surface layers. In contrast, the total amount of carbon-containing species decreased with increasing probing depth, because the C-species were located at the surface of the catalyst.

One should note that according to the XRD pattern in Fig. 2 the 13CuNi-$ZrO_2$50 catalyst may also include large *monometallic* Ni and Cu (unalloyed) particles. However, the Cu particles have very low activity and also the large Ni particles (with very low dispersion) have only a minor contribution to the overall reaction rate. With respect to the XPS measurements, the monometallic particles would also not contribute to the observed changes of surface composition (relative amount of Ni vs Cu) because monometallic particles apparently cannot contribute to segregation processes. If they would sinter at higher T, then the XPS signals should decrease but in fact the signals increase.

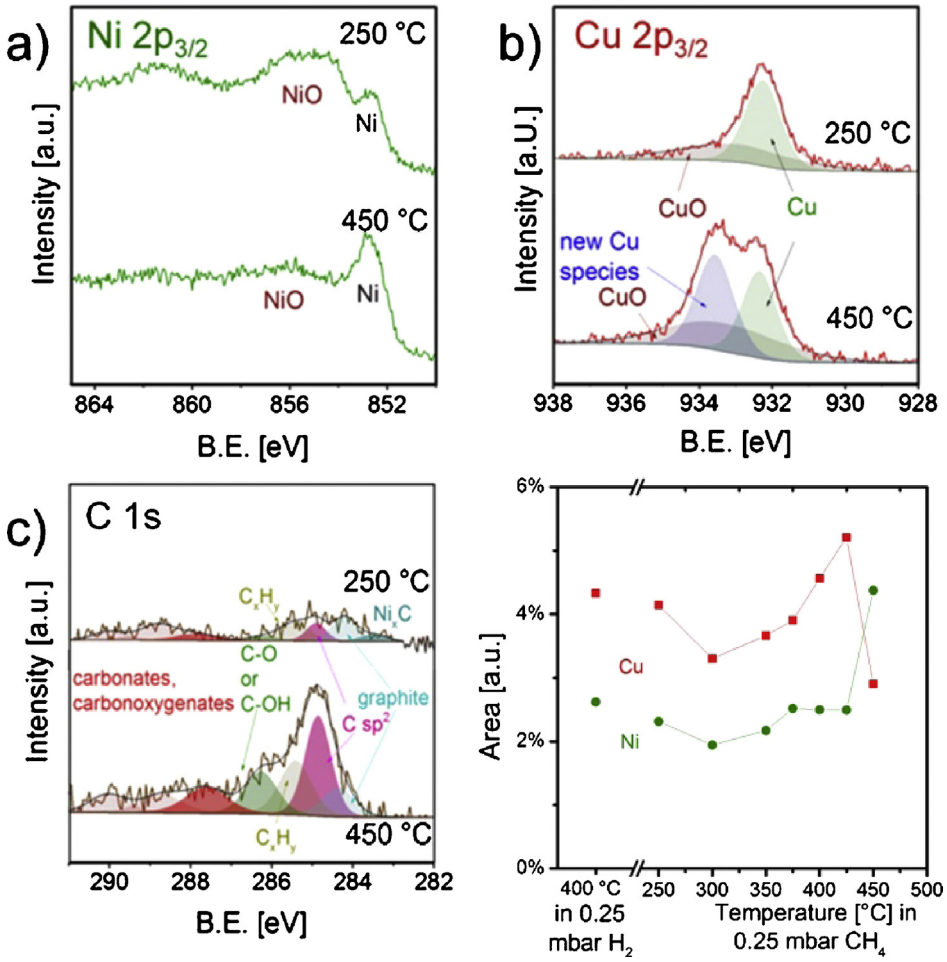

Fig. 8. XP spectra of the a) Ni $2p_{3/2}$ b) Cu $2p_{3/2}$ and c) C 1s core level region of 13CuNi-$ZrO_2$50 at 250 °C and 400 °C during heating in 0.25 mbar CH_4; and d) peak areas under consideration of cross section areas and normalized to simultaneously measured XPS peak areas of the Zr 3d region. The kinetic energy of the photoelectrons was 150 eV. Adapted from [11] –Published by The Royal Society of Chemistry.

Table 1
Adsorption energies E_{ads} (in eV) of CH_x species (x = 0–3) on fcc threefold hollow sites on Cu(111) and Ni(111) terraces of the $Cu_{70}Ni_{70}$ NP with optimized chemical ordering. The difference $\Delta E_{ads} = E_{ads}(fcc\text{-}Cu_3) - E_{ads}(fcc\text{-}Ni_3)$ between the adsorption energies for each adsorbed moiety is shown in a separate column.

Adsorbate	E_{ads} fcc-Cu_3	E_{ads} fcc-Ni_3	ΔE_{ads}
CH_3	−1.47	−1.97	0.50
CH_2	−3.09	−4.08	0.99
CH	−4.91	−6.44	1.53
C	−5.03	−7.02	1.99

We also carried out theoretical calculations to analyze whether CH_x species (x = 0–3) that form during methane decomposition can induce the segregation of Ni on the surface of nanoparticles. For this purpose we studied the adsorption of such CH_x species on Cu- and Ni-terraces in the $Cu_{70}Ni_{70}$ NP with optimized chemical ordering. This specific nanoparticle composition was selected, since in the minimum-energy structure it contains both Cu and Ni atoms on the facets (Fig. 5).

It is known from previous theoretical studies that the adsorption of CH_x groups is preferred on hollow sites compared to bridge or on-top positions on both Cu (111) and Ni(111) surfaces [73–78], hence we studied the CH_x adsorption exclusively on *fcc*-hollow sites on both Cu(111) and Ni(111) terraces of the $Cu_{70}Ni_{70}$ NP. As expected, we found that all CH_x groups are more strongly adsorbed on Ni(111) than on Cu(111). The difference between the adsorption energies of CH_x on Ni_3 and Cu_3 sites increases in the $CH_3 < CH_2 < CH < C$ order, being only 0.50 eV for a CH_3 group and ca. 2.0 eV for a single C atom (Table 1).

In order to evaluate to which extent such differences in adsorption energies can facilitate adsorbate-induced Ni-segregation on the surface we compared these differences with the energy required for Ni-segregation according to the topological energy expression of $Cu_{70}Ni_{70}$. We calculated the energy change for swapping 3 Ni atoms in the bulk with 3 Cu terrace atoms in the most stable $Cu_{70}Ni_{70}$ structure, which creates a Ni_3 hollow adsorption site replacing a Cu_3 site. Note that in the global minimum homotop of $Cu_{70}Ni_{70}$ the nanoparticle interior consists purely of Ni (Fig. 5), hence swapping 3 Ni and Cu atoms also implies increase in the number of Cu-Ni heteroatomic bonds within the NP (by 27 in this case). According to the topological expression of $Cu_{70}Ni_{70}$, the energy loss associated with the segregation of a Ni atom on the surface is 120 meV, and the formation of each Cu-Ni bond results in an energy loss of 11 meV. Therefore, the total energy loss corresponding to the segregation of 3 Ni atoms on a Cu(111) terrace is $3 \times 120 + 27 \times 11 = 657$ meV, or 219 meV per Ni atom.

The latter energies can be compared with ΔE_{ads} values from Table 1. For instance, a CH_3 group is adsorbed 0.5 eV stronger on the Ni_3 than on the Cu_3 site, which is sufficient to induce segregation of ~2 Ni atoms on the surface (2×219 meV = 0.438 eV). A C atom is adsorbed stronger on a Ni_3 than on a Cu_3 hollow site by as much as ~2.0 eV (Table 1) that is more than enough to induce the formation of a whole Ni_3 site on the surface. In summary, even the relatively weak adsorption of a CH_3 group can induce the segregation of Ni on the surface to a certain extent, whereas other stronger adsorbed CH_x species can more significantly facilitate such segregation (Fig. 9).

To summarize, the conclusions of the theoretical analysis are fully consistent with the experimental *operando* observations. In particular, simulations explain why increase in the temperature as well as the possible adsorption of CH_x moieties formed during CH_4 decomposition may induce Ni segregation on the surface.

Altogether one could now envision an "ideal" CuNi alloy particle. We know that, independent of the overall composition, after synthesis and activation (oxidation/reduction) a Cu-rich surface is obtained, but under reaction conditions Ni segregates on the surface. If the amount of Ni in the NP is sufficient to create a (nearly) complete Ni surface, then there is no (or less) coking resistance (due to the absence of surface Cu). Thus, an "ideal" nanoparticle would have Cu at edges and corners, and Ni at terraces. In turn, the interior of this nanoparticle would fully consist of Cu so that Ni segregation is limited (to maximize the resistance to coking). For example, to satisfy these conditions a ~6 nm large truncated octahedral $Cu_xNi_{3275\text{-}x}$ NP would have to contain 840 Ni atoms, i.e. the number of terrace positions in this NP (with Cu atoms occupying 180 edge/corner positions and 2255 interior sites). In the global minimum structure of the truncated octahedral particle $Cu_{2435}Ni_{840}$ at 0 K all aforementioned Ni atoms would be located in the NP interior. Since $Cu_{2435}Ni_{840}$ corresponds to the ca. Cu:Ni 3:1 composition, we can apply the descriptors obtained for $Cu_{105}Ni_{35}$ (see Supporting Information) to calculate the energy needed for the segregation of these 840 Ni atoms on the surface. The seemingly huge energy value of 166 eV, obtained in such a way can be easily compensated for by the adsorption of CH_x groups on the surface. According to Table 1, for instance 332 CH_3 groups adsorbed on the surface (at 0.4 ML terrace coverage) may provide enough energy for such segregation. However, such high coverage would introduce repulsion between methyl groups unaccounted for in this simple consideration. Thus, CH_3 groups are expected to induce only partial surface segregation of Ni in this composition. In the case of more strongly adsorbed CH_x groups, significantly lower coverage would be necessary to provide the energy for Ni segregation; hence the latter groups might induce the formation of purely Ni terraces in $Cu_{2435}Ni_{840}$. Indeed, a catalyst prepared with nominal Cu:Ni 3:1 composition exhibited a *specific* activity (per gram Ni) for H_2 production very similar to that of Ni-ZrO_2 but had much better coke resistance [11]. Based on temperature-programmed oxidation the amount of coke formed on the 3:1 bimetallic nanoparticles was reduced up to 50% and could also be reoxidized at ~100 °C lower temperature.

4. Conclusion

We have investigated the surface chemistry of bimetallic CuNi-ZrO_2 catalysts with a focus on the stable surface composition under specific reaction conditions, i.e. high temperatures and reactive methane atmosphere. Using FTIR spectroscopy, with CO as a probe molecule, and synchrotron-based NAP-XPS in hydrogen atmosphere we could observe that the surface was enriched in Cu upon reduction, even when the nanoparticles were rich in Ni. DF calculations confirmed that in thermodynamic equilibrium Cu tends to occupy surface sites on bimetallic Cu-Ni nanoparticles. For methane decomposition, *operando* studies of the surface composition of the catalyst and the nature of carbonaceous species on its surface were again performed using NAP-XPS. Between 425 and 450 °C, when H_2 production set in for CuNi-ZrO_2, significant changes in the XP spectra were observed caused by surface segregation of Ni. C 1s core level spectra revealed the appearance of various carbonaceous species on the catalyst surface at that temperature. In particular, the signal attributed to sp^2 carbon increased when activity set in. According to depth profiling, the carbonaceous species are mainly located at the surface layer. DF calculations showed that both the increase in temperature and the presence of CH_x groups on the catalyst surface can induce the segregation of Ni atoms on the surface. More dehydrogenated CH_x groups adsorb more strongly on Cu-Ni nanoparticles and, hence, have stronger effect on surface segregation. Whereas CH_3 species may induce only partial segregation of Ni on the surface of Cu-Ni nanoparticles, the presence of sufficient amounts of other species (CH_2, CH and C) adsorbed on the catalyst is calculated to result in the formation of purely Ni terraces. As a key result we conclude that independent of the initial Cu:Ni

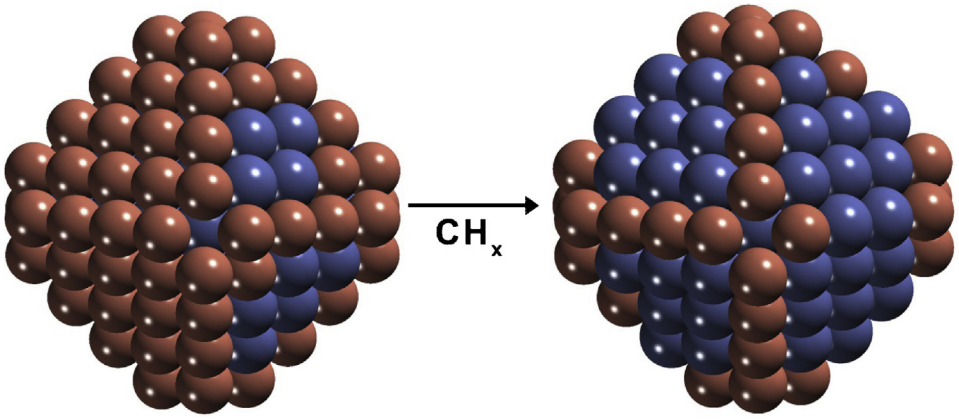

Fig. 9. Illustration of Ni segregation on the surface in $Cu_{70}Ni_{70}$ induced by CH_x groups. Cu atoms are displayed as redwood spheres and Ni atoms are shown as blue spheres. (For interpretation of the references to colour in this figure legend, the reader is referred to the web version of this article.)

ratio the nanoparticle surface is Cu rich after synthesis and reduction but it changes under reactive conditions when Ni is driven to the surface. This effect must be accounted for by catalyst synthesis, limiting the amount of Ni so that the anti-coking effect of Cu is preserved.

To achieve a better control of the desired surface composition of the bimetallic phases, it is essential to perform further *operando* and *computational* studies providing a detailed understanding of the nanoparticle stability in the reaction environment.

Acknowledgements

This work was supported by the Austrian Science Fund (FWF) under projects F4502-N16 and F4503-N16 (SFB FOXSI) and I942-N17 (DryRef). We thank HZB for the allocation of synchrotron radiation beamtime and we would like to thank the BESSY staff for assistance. The research leading to these results has received funding from the European Community's Seventh Framework Programme (FP7/2007-2013) under grant agreement N.°312284. The work of the Barcelona team was supported by the European Commission (FP7-NMP.2012.1.1-1 project ChipCAT, Reference No. 310191), Spanish MINECO (grants CTQ2012-34969 and CTQ2015-64618-R, co-funded by FEDER) and Generalitat de Catalunya (grants 2014SGR97 and XRQTC). Computer resources, technical expertise and assistance were provided by the Red Española de Supercomputación.

Appendix A. Supplementary data

Supplementary data associated with this article can be found, in the online version, at http://dx.doi.org/10.1016/j.cattod.2016.04.022.

References

[1] G. Rupprechter, C. Weilach, Nano Today 2 (2007) 20–29.
[2] S. Zafeiratos, S. Piccinin, D. Teschner, Catal. Sci. Technol. 2 (2012) 1787–1801.
[3] K. Föttinger, G. Rupprechter, Acc. Chem. Res. 47 (2014) 3071–3079.
[4] I. Gavrielatos, V. Drakopoulos, S.G. Neophytides, J. Catal. 259 (2008) 75–84.
[5] A.M. Molenbroek, J.K. Norskov, B.S. Clausen, J. Phys. Chem. B 105 (2001) 5450–5458.
[6] J. Ashok, M. Subrahmanyam, A. Venugopal, Int. J. Hydrogen Energy 33 (2008) 2704–2713.
[7] E.W. Park, H. Moon, M.-S. Park, S.H. Hyun, Int. J. Hydrogen Energy 34 (2009) 5537–5545.
[8] Y. Echegoyen, I. Suelves, M.J. Lazaro, R. Moliner, J.M. Palacios, J. Power Sources 169 (2007) 150–157.
[9] A.F. Cunha, J.J.M. Órfão, J.L. Figueiredo, Int. J. Hydrogen Energy 34 (2009) 4763–4772.
[10] A. Kitla, O.V. Safonova, K. Föttinger, Catal. Lett. 143 (2013) 517–530.
[11] A. Wolfbeisser, B. Klötzer, L. Mayr, R. Rameshan, D. Zemlyanov, J. Bernardi, K. Föttinger, G. Rupprechter, Catal. Sci. Technol. 5 (2015) 967–978.
[12] B. Li, S. Kado, Y. Mukainakano, T. Miyazawa, T. Miyao, S. Naito, K. Okumura, K. Kunimori, K. Tomishige, J. Catal. 245 (2007) 144–155.
[13] J.R. Rostrup-Nielsen, J. Sehested, J.K. Nørskov, Adv. Catal. 47 (2002) 65–139.
[14] J.R.H. Ross, A.N.J. van Keulen, M.E.S. Hegarty, K. Seshan, Catal. Today 30 (1996) 193–199.
[15] J.M. Wei, B.Q. Xu, J.L. Li, Z.X. Cheng, Q.M. Zhu, Appl. Catal. A 196 (2000) L167–L172.
[16] X.X. Zhang, Z.Q. Li, G.H. Wen, K.K. Fung, J. Chen, Y. Li, Chem. Phys. Lett. 333 (2001) 509–514.
[17] Y. Li, J. Chen, L. Chang, J. Zhao, Stud. Surf. Sci. Catal. 118 (1998) 321–329.
[18] Y. Li, D. Li, G. Wang, Catal. Today 162 (2011) 1–48.
[19] M.-S. Liao, Q.-E. Zhang, J. Mol. Catal. A Chem. 136 (1998) 185–194.
[20] C.-T. Au, C.-F. Ng, M.-S. Liao, J. Catal. 185 (1999) 12–22.
[21] G. Rupprechter, Catal. Today 126 (2007) 3–17.
[22] K. Zorn, S. Giorgio, E. Halwax, C.R. Henry, H. Grönbeck, G. Rupprechter, J. Phys. Chem. C 115 (2011) 1103–1111.
[23] K. Föttinger, J.A. van Bokhoven, M. Nachtegaal, G. Rupprechter, J. Phys. Chem. Lett. 2 (2011) 428–433.
[24] A. Haghofer, K. Föttinger, F. Girgsdies, D. Teschner, A. Knop-Gericke, R. Schlögl, G. Rupprechter, J. Catal. 286 (2012) 13–21.
[25] K. Föttinger, Catal. Today 208 (2013) 106–112.
[26] C. Rameshan, W. Stadlmayr, S. Penner, H. Lorenz, N. Memmel, M. Hävecker, R. Blume, D. Teschner, T. Rocha, D. Zemlyanov, A. Knop-Gericke, R. Schlögl, B. Klötzer, Angew. Chem. Int. Ed. 51 (2012) 3002–3006, 1.
[27] C. Rameshan, W. Stadlmayr, C. Weilach, S. Penner, H. Lorenz, M. Hävecker, R. Blume, T. Rocha, D. Teschner, A. Knop-Gericke, R. Schlögl, N. Memmel, D. Zemlyanov, G. Rupprechter, B. Klötzer, Angew. Chem. Int. Ed. 49 (2010) 3224–3227, 1.
[28] H. Bluhm, M. Haevecker, A. Knop-Gericke, E. Kleimenov, R. Schlögl, D. Teschner, V.I. Bukhtiyarov, D.F. Ogletree, M. Salmeron, J. Phys. Chem. B 108 (2004) 14340–14347.
[29] J.J. Yeh, I. Lindau, At. Data Nucl. Data Tables 32 (1985) 1–155.
[30] G. Kresse, J. Furthmüller, Phys. Rev. B 54 (1996) 11169–11186.
[31] J.P. Perdew, K. Burke, M. Ernzerhof, Phys. Rev. Lett. 77 (1996) 3865–3868.
[32] P. Janthon, S.M. Kozlov, F. Viñes, J. Limtrakul, F. Illas, J. Chem. Theory Comput. 9 (2013) 1631–1640.
[33] M. Methfessel, A.T. Paxton, Phys. Rev. B 40 (1989) 3616–3621.
[34] S.M. Kozlov, H.A. Aleksandrov, J. Goniakowski, K.M. Neyman, J. Chem. Phys. 139 (2013) 084701.
[35] F. Viñes, F. Illas, K.M. Neyman, Angew. Chem. Int. Ed. 46 (2007) 7095–7097.
[36] Q. Wu, L.D.L. Duchstein, G.L. Chiarello, J.M. Christensen, C.D. Damsgaard, C.F. Elkjaer, J.B. Wagner, B. Temel, J.-D. Grunwaldt, A.D. Jensen, ChemCatChem 6 (2014) 301–310.
[37] A. Bandara, S. Dobashi, J. Kubota, K. Onda, A. Wada, K. Domen, C. Hirose, S.S. Kano, Surf. Sci. 387 (1997) 312–319.
[38] L. Bonneviot, F.X. Cai, M. Che, M. Kermarec, O. Legendre, C. Lepetit, D. Olivier, J. Phys. Chem. 91 (1987) 5912–5921.
[39] M. Kermarec, D. Olivier, M. Richard, M. Che, F. Bozon-Verduraz, J. Phys. Chem. 86 (1982) 2818–2827.
[40] J.A. Dalmon, M. Primet, G.A. Martin, B. Imelik, Surf. Sci. 50 (1975) 95–108.
[41] G. Blyholder, J. Phys. Chem. 68 (1964) 2772–2778.
[42] K. Hadjiivanov, M. Mihaylov, D. Klissurski, P. Stefanov, N. Abadjieva, E. Vassileva, L. Mintchev, J. Catal. 185 (1999) 314–323.
[43] S.M. Vesecky, X. Xu, D.W. Goodman, J. Vac. Sci. Technol. A 12 (1994) 2114–2118.
[44] K. Hadjiivanov, H. Knözinger, M. Mihaylov, J. Phys. Chem. B 106 (2002) 2618–2624.
[45] P.H. Kasal, R.J. Bishop Jr., D. McLeod Jr., J. Phys. Chem. 82 (1978) 279–285.

[46] C. Morterra, E. Giamello, G. Cerrato, G. Centi, S. Perathoner, J. Catal. 179 (1998) 111–128.
[47] S. Chen, H. Zou, Z. Liu, W. Lin, Appl. Surf. Sci. 255 (2009) 6963–6967.
[48] A.A. Davydov, Infrared Spectroscopy of Adsorbed Species on the Surface of Transition Metal Oxides, John Wiley & Sons, Novosibirsk, USSR, 1984.
[49] M. Manzoli, M.R. Di, F. Boccuzzi, S. Coluccia, J. Kaspar, Appl. Catal. B 61 (2005) 192–205.
[50] M.M.V.M. Souza, D.A.G. Aranda, M. Schmal, J. Catal. 204 (2001) 498–511.
[51] M. Daturi, C. Binet, J.-C. Lavalley, A. Galtayries, R. Sporken, Phys. Chem. Chem. Phys. 1 (1999) 5717–5724.
[52] M. Mihaylov, K. Chakarova, K. Hadjiivanov, J. Catal. 228 (2004) 273–281.
[53] R.P. Eischens, Z. Elektrochem. 60 (1956) 782–788.
[54] L. Guczi, G. Stefler, O. Geszti, I. Sajo, Z. Paszti, A. Tompos, Z. Schay, Appl. Catal. A 375 (2010) 236–246.
[55] N.C. Triantafyllopoulos, S.G. Neophytides, J. Catal. 239 (2006) 187–199.
[56] W. Chia-Ching, Y. Cheng-Fu, Nanoscale Res. Lett. 8 (2013) 33.
[57] C.D. Wagner, W.M. Riggs, L.E. Davis, J.F. Moulder, Handbook of X-Ray Photoelectron Spectroscopy, 5534, Perkin-Elmer Corporation, Physical Electronics Division, Eden Prairie, Minnesota, 1979.
[58] B. Pawelec, S. Damyanova, K. Arishtirova, J.L.G. Fierro, L. Petrov, Appl. Catal. A 323 (2007) 188–201.
[59] L.-C. Chen, S.D. Lin, Appl. Catal. B 106 (2011) 639–649.
[60] A.R. Naghash, T.H. Etsell, S. Xu, Chem. Mater. 18 (2006) 2480–2488.
[61] S.D. Jones, L.M. Neal, H.E. Hagelin-Weaver, Appl. Catal. B 84 (2008) 631–642.
[62] J. Ghijsen, L.H. Tjeng, E.J. Van, H. Eskes, J. Westerink, G.A. Sawatzky, M.T. Czyzyk, Phys. Rev. B Condens. Matter 38 (1988) 11322–11330.
[63] Z. Liu, M.D. Amiridis, Y. Chen, J. Phys. Chem. B 109 (2005) 1251–1255.
[64] W. Tong, A. West, K. Cheung, K.-M. Yu, S.C.E. Tsang, ACS Catal. 3 (2013) 1231–1244.
[65] S.M. Kozlov, G. Kovács, R. Ferrando, K.M. Neyman, Chem. Sci. 6 (2015) 3868–3880.
[66] E. Panizon, J.A. Olmos-Asar, M. Peressi, R. Ferrando, Study of structures and thermodynamics of CuNi nanoalloys using a new DFT-fitted atomistic potential, Phys. Chem. Chem. Phys. 17 (2015), http://dx.doi.org/10.1039/C5CP00215J (28407–28407).
[67] G. Kovács, S.M. Kozlov, I. Matolinova, M. Vorokhta, V. Matolin, K.M. Neyman, Phys. Chem. Chem. Phys. 17 (2015) 28298–28310.
[68] S.T. Jackson, R.G. Nuzzo, Appl. Surf. Sci. 90 (1995) 195–203.
[69] G.J. Kovács, I. Bertóti, G. Radnóczi, Thin Solid Films 516 (2008) 7942–7946.
[70] P.G. Savva, K. Polychronopoulou, V.A. Ryzkov, A.M. Efstathiou, Appl. Catal. B 93 (2010) 314–324.
[71] J.I.B. Wilson, J.S. Walton, G. Beamson, J. Electron Spectrosc. Relat. Phenom. 121 (2001) 183–201.
[72] F. Studt, F. Abild-Pedersen, Q. Wu, A.D. Jensen, B. Temel, J.-D. Grunwaldt, J.K. Nørskov, J. Catal. 293 (2012) 51–60.
[73] K. Li, C. He, M. Jiao, Y. Wang, Z. Wu, Carbon 74 (2014) 255–265.
[74] G. Gajewski, C.-W. Pao, J. Chem. Phys. 135 (2011) 064707.
[75] J.E. Müller, A.C.T. van Duin, W.A. Goddard, J. Phys. Chem. C 113 (2009) 20290–20306.
[76] S.-G. Wang, D.-B. Cao, Y.-W. Li, J. Wang, H. Jiao, J. Phys. Chem. B 110 (2006) 9976–9983.
[77] W. Zhang, P. Wu, Z. Li, J. Yang, J. Phys. Chem. C 115 (2011) 17782–17787.
[78] Y.-A. Zhu, D. Chen, X.-G. Zhou, W.-K. Yuan, Catal. Today 148 (2009) 260–267.